

Scattering-assisted localization microscopy

Marco Leonetti^{1,2}, Alfonso Grimaldi¹, Giancarlo Ruocco^{1,3}, Giuseppe Antonacci¹

¹Center for Life Nano science @ Sapienza, Istituto Italiano di Tecnologia, Viale Regina Elena, 291, I-00161 Roma, Italia

²CNR NANOTEC, Istituto di Nanotecnologia, I-73100 Lecce, Italia and

³Dipartimento di Fisica, Università "La Sapienza", Piazzale Aldo Moro, 5, I-00185 Roma, Italia

Super-resolution fluorescence microscopy techniques break the diffraction limit in biological systems, promising a resolution ultimately limited only by the size of the emitting molecules. These methods, however, demand high numerical aperture (NA) lenses, in turn involving short working distances (typically below 1mm), while their imaging capability rapidly decays in turbid samples. Here we demonstrate that the unavoidable light scattering arising in biosystems can be exploited to generate sub-diffraction images using low NA and long working distances. In the Scattering-Assisted localization Microscopy (SAM), the resolution is defined by the grain size of the speckle pattern on a sample rather than by the collection optics. We report a four-fold increase in resolution compared to the theoretical diffraction limit, enabling, as an example, the detection of micron-sized Beta Amyloid plaques in brain tissues using a lens of 25 mm working distance and minimal laser power.

I. INTRODUCTION

The diffraction limit sets a fundamental limit in the spatial resolution achievable by an imaging system. According to the Abbe¹ and the Rayleigh² criteria, the larger the solid angles of the illumination and collection optics, the higher the spatial resolution achievable by the imaging system. A high NA is indeed an essential ingredient in most imaging schemes, such as Confocal³, Structured Illumination⁴, Stimulated Emission Depletion⁵ and Photoactivated Localization Microscopy^{6,7}. Ideally, the maximum resolution achievable through conventional optics requires a lens in contact with the sample, which represents a severe limitation in non-invasive and in-vivo measurements. In biological systems, the unavoidable light scattering degrades the wavefront shape and introduce optical aberrations^{8,9}, in turn limiting the achievable resolution due to diffusion which scrambles light rays into uncorrelated optical paths.

Recently, wavefront shaping methods, demonstrated the possibility to focus light onto a single grain of a disorganized speckle pattern^{10–12}. These “enhanced speckle grains” (HSG) are obtained building constructive interference out of a randomized field¹³, where the wavefront of the incident beam is modulated by spatial light modulators¹⁴ or digital micro-mirror devices (DMD)¹⁵ and processed through feedback algorithms. The size of a HSG in the disordered medium corresponds to the average grain size of the speckle pattern, and is independent from the illumination and collection optics¹⁰. Wavefront shaping and the HSGs are today fundamental in a plethora of applications ranging from drug activation¹⁶ to deep neuronal stimulation¹⁷, and have been also employed for imaging^{18–20} taking advantage of “opaque lenses”.

Here, we demonstrate the use of wavefront shaping to achieve a four fold increase of imaging resolution with respect to the diffraction limit of the imaging lens in semi-transparent and turbid biological samples. SAM relies on the diffraction-free size of the HSGs that is indepen-

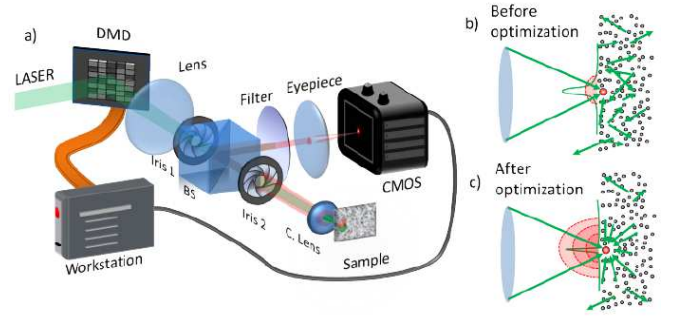


FIG. 1: **Principle and schematic of SAM** a) Schematic of the experimental setup. A CW laser beam (~ 0.1 mW optical power at $\lambda = 532$ nm) is modulated by a DMD and focused to the sample by a lens (L1) of 25 mm focal length. Fluorescent light from the sample is collected by the same illumination lens and detected by an CMOS camera. The Irises serve to perform experiments with variable NA ($0 < \text{NA} < 0.25$). Iris 1 (placed before the beamsplitter) controls only excitation beam, while Iris 2 controls both excitation and collection NA. b) In standard wide field imaging, the size of the focal spot is given by the diffraction limit of the illumination lens. c) In SAM microscopy, the resolution is increased controlling light paths of large k -vectors naturally generated by the scattering in the medium.

dent from the system NA and is limited to $\Omega = \lambda/2$ in the far field²¹, (where λ is the light wavelength) while may be smaller inside the volume of an highly scattering medium^{22,23}. Our wavefront shaping technique maximizes the fluorescent signal through a guide-star optimization²⁴ from a target T on the surface or embedded into the sample. Once the optimization is completed, the fluorescent signal excited by the optimized speckle is localized²⁵ by fitting the resulting point spread function. This process is repeated for an ensemble of targets covering the entire field of view, enabling the reconstruction of a speckle-defined high-resolution image.

Fig. 1 shows the experimental setup (Fig. 1a) and

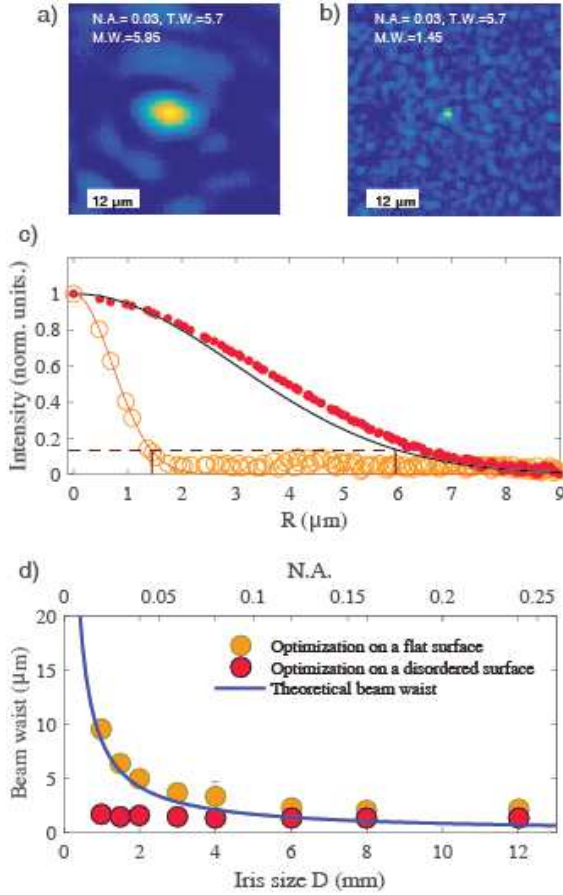


FIG. 2: **Speckle resolution.** Focus obtained by wavefront shaping on a polished glass surface with limited illumination numerical aperture (Iris 1 closed) (a) and in a disordered medium (b). The sharper focus is the result of the increased number of k-vectors generated by the scattering medium. Theoretical (T.W.) and measured (M.W.) beam waist are reported. c) Intensity profiles for the two cases, where the black solid line represents the theoretical profile for $NA=0.03$ and the thin solid line is a Gaussian fit of the HSG data. d) Plot of the beam waist as a function of both the aperture diameter and the associated illumination NAs. Whilst the waist on the polished surface follows the theoretical limit (solid line), the one on the disordered medium remains constantly low even at low NAs.

illustrated the principles (Fig. 1b,c) behind SAM microscopy. A DMD is used to modulate the wavefront of the incident beam. A CMOS camera detects the fluorescent signal emitted from a target region which is then processed by custom algorithms to perform a wavefront optimization.

To demonstrate that the HSGs size is independent from the NA of the focusing optics, we first compared the focus obtained after optimization on both a polished glass surface, where the speckles are mostly absent, and a disordered layer of scatterers (60 μm thick layer of TiO_2 particles) on a setup where excitation numerical aperture is controlled by acting on Iris 1 (and leaving Iris 2

fully open in order to affect only the illumination NA). The optimization algorithm flips one of the DMDs and monitors simultaneously intensity at a target. If the intensity increases, then the configuration is maintained, otherwise the previous orientation is restored. The size of the focal spot obtained at the smooth surface (Fig. 2a) is significantly larger than the one obtained on the granular surface (Fig. 2b), as further illustrated by the intensity profiles (Fig. 2c). The larger focal spot is a consequence of the limited number of k-vectors generated across the polished glass surface, where the wavefront optimization process has the effect of correcting only the optical aberrations of the objective, as in conventional adaptive optics methods. By contrast, the HSG obtained at the disordered medium is the result of all the interfering k-vectors naturally generated by the light scattering and controlled by wavefront shaping. Fig. 2d shows the measured HSG size (FWHM) for different illumination NAs. While the beam waist obtained at the polished surface follows the theoretical limit dictated by the system NA, the one obtained from the disordered medium remains constant even at low NAs, as expected for a focus whose size is defined only by the scattering properties of the medium.

We exploited this concept to perform high-resolution imaging without the need of high NA lenses, and to do this we will control both collection and focusing NA by acting on Iris 2 while leaving Iris 1 fully open. Fig. 3 illustrates the image reconstruction process of SAM. During the optimization process, the fluorescent signal emitted from a single location T in the field of view of coordinates $[x_T, y_T]$ works as a local intensity report, i.e. if the fluorescence intensity increases after the flipping of one of the DMD micromirrors than the configuration is maintained, otherwise the previous one is restored to the original orientation. Iteration of this process through all the illuminated DMD micromirrors, produces a fluorescence enhancement which is originated by an HSG overlapping with fluorescent molecules close to T . The presence of multiple HSG (which can be in principle detrimental for the resolution) with the same intensity is an extremely rare event as shown in the **supplementary information**. The final position of the HSG is not necessarily corresponding to T as it depends on the overlap between the fluorescent signal and T . Once the optimization process is completed (three examples in Fig. 3c₁₋₃), we subtract to the optimized fluorescence signal the signal taken prior to optimization obtaining the signal deriving only from the HSG (Fig. 3d₁₋₃) with total intensity I_N . This feature appears with a size larger than its real extension due to convolution with the collection optics (Fig. 3a). To localize the HSG, we perform a Gaussian fit of the resulting intensity profile, providing the center coordinates X'_N and Y'_N . Consequently, a frame is reconstructed (Fig. 3b) containing a Gaussian distribution of the intensity with center coordinates X'_N and Y'_N , total intensity I_N , and waist equal to the average size of the HSG in the sample (which has been previously

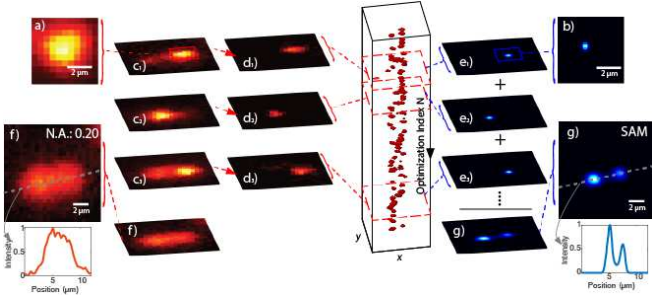


FIG. 3: **Image reconstruction process.** Fluorescence generated by an HSG at the end of the optimization process is shown in (a). The process is iterated many times using different targets (panels c_{1-3}), from which the HSG signal is retrieved by subtracting the non optimized fluorescence (panels d_{1-3}). We retrieve a frame for each iteration N subtracting the background signal due to the non optimized fluorescence localizing the HSG through a Gaussian fit, as illustrated in panels e_{1-3} (zoom of e_1 reported in panel b). A schematic representation of the process is shown in the central panel, where each stack N is illustrated for multiple optimizations. The final image (g) is obtained summing all the reconstructed frames. For comparison, panel f) shows the image obtained by summing bare fluorescence signal. The sub-panels of e) and f) show the resulting intensity profiles along the dashed line.

characterized, **see supplementary information**). The optimization is repeated several times for all the set of targets $\{T\}$ which are defined by the user in order to cover the whole region of interest with a density close to A_{ROI}/A_{HSG} , where A_{ROI} is the area of the region of interest and A_{HSG} is the area of an HSG. Each optimization produces an HSG at a different locations, from which we obtain an associated stack of frames of superlocalized spots (Fig. 3d₁₋₃). All frames are then summed together to yield the final image (Fig. 3g). As a result, the final resolution is higher than the one given by conventional imaging, as shown in Fig. 3f for comparison.

II. RESULTS

The enhanced resolution of SAM, is demonstrated imaging two small ($0.5 \mu m$ diameter) neighboring fluorescent beads on a titanium dioxide layer (**see methods**) with a 0.2 NA objective (nominal resolution $1.36 \mu m$). The two beads appear as a single elongated structure (Fig. 4a) when imaged with a low NA lens. By contrast, the reconstructed SAM image clearly resolves the two beads (Fig. 4b), as further illustrated by the cross sectional intensity profiles (Fig. 4c). We measured a resolution of ~ 312 nm (**see supplementary information**) corresponding to a more than four-fold enhancement in the spatial resolution. By decreasing the effective NA of the lens (Fig. 4d), the two beads remained clearly distinguishable after the SAM reconstruction (Fig. 4e,f). A further decrease in the NA (Fig. 4g) brings the fluores-

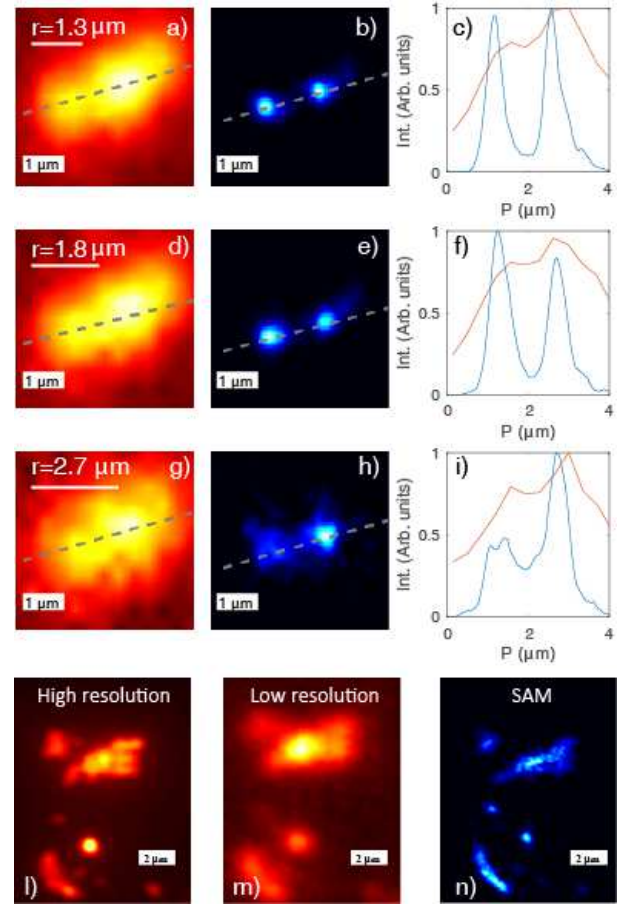


FIG. 4: **SAM imaging.** Two beads of $0.5 \mu m$ diameter were imaged on a $60 \mu m$ titanium dioxide substrate in a standard configuration (a) and with SAM microscopy (b) with a system $NA=0.2$. White bar on the upper left of the panel indicates the optical resolution r . c) Intensity profile along the grey lines. The orange and blue lines are relative to the standard and SAM image respectively. The same sequence is reported in d-f) where measurements were performed with $NA=0.15$, and for panels g-i) with $NA=0.12$. l-m) Images of amyloid plaques in a $250 \mu m$ brain slice obtained in a standard configuration with a high $NA=0.75$ (l) and a low $NA=0.2$ objective (m). n) Reconstructed SAM image obtained with the low resolution objective lens, highlighting the enhanced resolution with respect to the image obtained by the standard configuration.

cence intensity close to the noise level, thereby degrading the SAM image quality (Fig. 4h,i).

To demonstrate the capability of SAM microscopy to perform imaging on standard semi-transparent biological tissues, we performed measurements on brain slices, containing Amyloid Beta plaques tagged with a fluorescent marker. We used slices derived from a mouse model of the Alzheimer's disease (**see methods**), where we first performed immunofluorescence imaging to detect the presence of Amyloid Beta plaques. High resolution (obtained with $NA=0.75$), low resolution (obtained with $NA=0.2$) and SAM microscopy images (obtained with $NA=0.2$) of

the Amyloid Beta plaques are reported in Fig. 4l, m and n respectively. We retrieve a resolution of 346 nm.

III. DISCUSSION

SAM microscopy provides an increased resolution without the need of high power laser beams or pulsed sources, while blinking or photo switchable fluorescent chemical compounds are unnecessary. The relative simplicity of the experimental setup makes the proposed approach very general as it can be applied to any fluorescence imaging scheme. Since the resolution limit is driven by the size of the speckle grain, the proposed technique shows its maximum advantage in experiments where high resolution is needed together with a long working distance, a condition that is currently forbidden by the physical NA of the illumination and collection optics. Involving minimal optical power, SAM can be a powerful tool for the investigation of systems with low damage threshold, and may be easily exported or to in vivo investigation of sensible tissues such as the human retina.

IV. METHODS

A. Wavefront shaping intensity optimization protocol

We follow a sequential scan optimization protocol similar to that described in previous reports^{11,15}. The DMD (Vialux Discovery 4100) is organized into 11×11 square segments each of $70 \mu\text{m}$ side. The laser beam illuminates the active area of the DMD. Once a Region of interest of the camera is selected as a target, one segment (randomly chosen) of the DMD is flipped. The pixel intensity in the new frame is then compared with the associated value of the previous frame. The change is accepted if the intensity is increased, otherwise the change is discarded and the previous configuration is restored. This operation is repeated for neighboring active segments of the DMD. Exposure time varies from 2 to $40 \mu\text{s}$, and optimization is carried for a minimum of 60 active segments for each optimization target. The average time to focus light at a

target is approximately 0.65 seconds.

B. Scattering sample preparation

A 60 micron layer of titanium dioxide (Sigma Aldrich, N.224227) was prepared in an ethanol suspension and deposited on a glass coverslip. The layer thickness has been measured by an analogical profilometer. To perform resolution measurements, we used fluorescent beads (Spherotech FP-00556-2) of $0.5 \mu\text{m}$ diameter.

C. Brain slice preparation

All experiments on animals were conducted in conformity with European Directive 2010/63/EU and the Italian D.lg. 4.05.2014 and all methods were carried out in accordance with relevant guidelines and regulations. One year old 3xTg-AD mice were euthanized and transcardially perfused with cold Phosphate Buffered Saline (PBS) solution. $300 \mu\text{m}$ thick slices were obtained with a vibratome. Slices were fixed in a 4% Paraformaldehyde solution for 16 hours at 4°C and then processed for the free-floating immunostaining. Slices were treated with a solution of 70% formic acid for 30 minutes to reveal antigen and then blocked with 3% goat serum and 0.3% Triton X-100 in PBS for 1 hour; Amyloid Beta-recognizing primary antibody (803001, Biolegend) was added 1:100 in a solution of 1% goat serum and 0.1% Triton X-100 in PBS at 4°C for 16 hours in continuous agitation. After 3 washes in PBS, Goat anti-Mouse IgG (H&L) Coated Fluorescent Nile Red secondary antibody (MFP-0556-5, Spherotech) was added for 1h and then the last 3 washes in PBS were performed. Stained brain slices were mounted on a slide with a fluorescent mounting medium and covered with a coverslips.

D. SAM image reconstruction

The image shown in Fig. 4n was obtained performing a total of 1288 (46×28) optimizations, for a total acquisition time of 850 seconds.

-
- [1] E. Abbe, *Archiv für mikroskopische Anatomie* **9**, 413 (1873).
 - [2] L. Rayleigh, *Journal of the Royal Microscopical Society* **23**, 474 (1903).
 - [3] J. B. Pawley, *Fundamental Limits in Confocal Microscopy* (Springer US, Boston, MA, 2006), pp. 20–42.
 - [4] M. G. Gustafsson, *Journal of microscopy* **198**, 82 (2000).
 - [5] S. W. Hell and J. Wichmann, *Optics letters* **19**, 780 (1994).
 - [6] E. Betzig, G. H. Patterson, R. Sougrat, O. W. Lindwasser, S. Olenych, J. S. Bonifacio, M. W. Davidson, J. Lippincott-Schwartz, and H. F. Hess, *Science* **313**, 1642 (2006).
 - [7] P. P. Mondal and A. Diaspro, in *Fundamentals of Fluorescence Microscopy* (Springer, 2014), pp. 161–187.
 - [8] P. Sebbah, *Waves and imaging through complex media* (Springer Science & Business Media, 2012).
 - [9] C. K. Hayakawa, V. Venugopalan, V. V. Krishnamachari, and E. O. Potma, *Physical review letters* **103**, 043903 (2009).
 - [10] I. M. Vellekoop, A. Lagendijk, and A. Mosk, *Nature photonics* **4**, 320 (2010).

- [11] I. M. Vellekoop and A. Mosk, Optics letters **32**, 2309 (2007).
- [12] D. Di Battista, G. Zacharakis, and M. Leonetti, Scientific reports **5**, 17406 (2015).
- [13] I. Vellekoop and A. Mosk, Optics communications **281**, 3071 (2008).
- [14] N. Savage, Nature Photonics **3**, 170 (2009).
- [15] D. Akbulut, T. J. Huisman, E. G. van Putten, W. L. Vos, and A. P. Mosk, Optics express **19**, 4017 (2011).
- [16] Z. Huang, Technology in cancer research & treatment **4**, 283 (2005).
- [17] F. Zhang, V. Gradinaru, A. R. Adamantidis, R. Durand, R. D. Airan, L. de Lecea, and K. Deisseroth, Nature protocols **5**, 439 (2010).
- [18] I. M. Vellekoop and C. M. Aegerter, Optics letters **35**, 1245 (2010).
- [19] H. Yilmaz, E. G. van Putten, J. Bertolotti, A. Lagendijk, W. L. Vos, and A. P. Mosk, Optica **2**, 424 (2015).
- [20] E. Van Putten, D. Akbulut, J. Bertolotti, W. Vos, A. Lagendijk, and A. Mosk, Physical review letters **106**, 193905 (2011).
- [21] J. W. Goodman, *Speckle phenomena in optics: theory and applications* (Roberts and Company Publishers, 2007).
- [22] R. Carminati, Physical Review A **81**, 053804 (2010).
- [23] J.-H. Park, C. Park, H. Yu, J. Park, S. Han, J. Shin, S. H. Ko, K. T. Nam, Y.-H. Cho, and Y. Park, Nature photonics **7**, 454 (2013).
- [24] R. Horstmeyer, H. Ruan, and C. Yang, Nature photonics **9**, 563 (2015).
- [25] M. A. Thompson, M. D. Lew, and W. Moerner, Annual review of biophysics **41**, 321 (2012).